Capacitive Displacement Sensor for a Self-Sensing Shock-Absorber Piston-Cylinder Mechanism

Capacitive Displacement Sensor for a Self-Sensing Shock-Absorber Piston-Cylinder Mechanism

1st Dario Gandini
Department of Electronics and Telecommunication (DET)
Politecnico di Torino
Turin, Italy

2nd Pierpaolo Sorbellini
Department of Electronics and Telecommunication (DET)
Politecnico di Torino
Turin, Italy

3rd Marcello Chiaberge
Department of Electronics and Telecommunication (DET)
Politecnico di Torino
Turin, Italy
marcello.chiaberge@polito.it

4th Simone Marchetti
Marelli Ride Dynamics
Turin, Italy

5th Marco di Vittorio
Marelli Ride Dynamics
Turin, Italy

6th Giordano Greco
Marelli Ride Dynamics
Turin, Italy

7th Piero Monchiero
Marelli Ride Dynamics
Turin, Italy

***Abstract*—Measurement of piston displacement is a common problem for any pneumatic or hydraulic device, like shock-absorber. Direct measurements are not always feasible because of mechanical constraints; most recent techniques rely on magnetic phenomena, introducing considerable complexity. In an attempt to achieve an economical and feasible solution, an intrinsic capacitive sensor is developed. Such sensors measure the capacitance between piston and cylinder, which is directly proportional to displacement. It is developed an oscillator stage to measure the unknown capacitance. The oscillator's output is acquired by a microcontroller, conditioned and transformed into the estimated displacement. This paper focuses on the design methodology of the measurement stage, highlighting tradeoffs and optimizations. The sensor was developed for an automotive application in a commercial shock absorber: however, it can be extended to other devices where proper electrical isolation between cylinder and piston is provided. Mathematical models and experimental results are reported compared to a commercial position sensor.**

***Index Terms*—Capacitive sensors, Displacement measurement, Pistons, Position measurement, Shock-absorbers**

I. Introduction

THE problem of measuring the position of a piston rod, inside a cylinder, arises in many hydraulic or pneumatic devices, in the automotive field this mechanics is present in the shock-absorber, Fig. 1. Measuring the displacement of the shock-absorber allow dynamics controls, e.g. headlight adjustment. Various types of sensors have been developed. String transducers must be mounted inside the cylinder, potentiometers can be placed inside or outside: they complicate the mechanical design and maintenance and they are subjected to wear. Optical and microwave position sensors are contactless but must be mounted inside the cylinder and have reliability issues [1]–[3]. Induction and magnetic sensors are more reliable and less invasive contactless technologies [4]. Induction sensors usually work by placing an outer coil on the cylinder and using a ferromagnetic material for the piston rod. The piston changes the coil's inductance with its position; however, having the entire cylinder covered with a coil could be expensive and uncomfortable, especially when the size increases. Moreover, eddy currents limit the dynamic range of the sensor, limiting the excitation frequency used [5]–[8]. [9] uses a magnet and a strip of hall-effect sensors on the cylinder as an alternative for small cylinders. However, a sensor strip along the direction of displacement is always required.

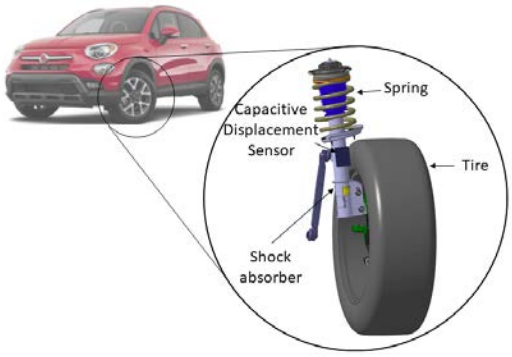

Fig. 1. Automotive Shock-Absorber simplified scheme

If the outer cylinder is made of non-ferromagnetic material, i.e. aluminium, it is possible to attach a permanent magnet to the piston and measure its field with a linear array of magnetic sensors placed on the cylinder: a non-ferromagnetic stainless steel rod is expensive, and the mechanical design and the mounting process are more complex. [10] proposes a sensing technique that detects the radial magnetic field associated with the end of a soft iron rod with some external fluxgate sensors and an external winding to produce the excitation. LVDT (Linear Variable Differential Transformer) sensors are made by a primary coil with an AC excitation placed on the cylinder, followed by two secondary coils in series wrapped in the opposite direction; in this case, the ferromagnetic rod creates a voltage on the secondary winding depending on the rod position; these coils are usually embedded in the cylinder structure [11]. Their drawbacks are the sensitivity to the temperature, the fact that the cylinder structure becomes more complex, and the rod material must have high permeability, but they are reliable. Recently [12] reduced the dimension of the excitation coil and the pick-up coils by introducing a conical rod, moving the cylinder winding complexity to the rod that must have some degree of accuracy in manufacturing the cylindrical shape. In any case, all the technique that relies on the sensing of the magnetic field can be disturbed by any external field coming from the environment. Eventually, [13] proposes some algorithms to correct the estimation produced by integrating a MEMS sensor placed on the rod, which does not require any particular modification of the mechanical assembly. However, after reaching a new set-point, a compensation phase is required to remove the integration error.

Here, a capacitive sensor is investigated to compute the displacement by measuring the capacitance between the cylinder and the piston rod. This approach reduces the costs: no coil, magnets, or sensor arrays are required. The mechanism piston-cylinder is a cylindrical capacitance by definition, and the geometry of the system itself is used to generate the measured capacitance. This approach has been no novelty since a patent submission in 1985 [14], whereas more recently, another relevant patent was published in 2009 [15], however, in general, the literature lacks of contributions about the correct design of this kind of solution, its feasibility and the accuracy of the measurements. Only recently, [16] published an article on a capacitive sensor for a biomedical device, and [17] proposed a similar technique for measuring shafts, either using some commercials' IC or development board as sensing circuit.

In this article, a feasible solution, from an industrial point of view, is presented, focusing on the design methodology and optimization. This intrinsic capacitive sensor is applied and tested on an automotive shock absorber, but that can be used in any piston-cylinder mechanism that features two main characteristics:

1) the cylinder and piston are made of conductive material.
2) the connection between piston and cylinder is made with a non-conductive material (i.e. they are not short-circuited).

This technology is designed for this application because the impact on the mechanical design is marginal and does not require introducing any particular element in the design (like windings or an array of sensors) that is crucial in an application with high production volume and the influence on the product's cost must be as lower as possible.

The following article is organized as follows: an overview of the equivalent capacitance model; a brief description of circuits to measure an unknown capacitor; the working principle and the mathematical modeling of the non-idealities of the chosen topology, and the design optimization together with the acquisition chain, last sections are dedicated to experimental results and conclusions. '

II. Shock Absorber Capacitance Model

The piston-cylinder mechanism is a capacitor by definition, two metal armors with a dielectric in between; the system's geometry defines the measured capacitor. The total capacitance, knowing the mechanical design, can be separated into different parallel capacitors with a defined geometry. The simplified model of a shock absorber Fig. 2 is used to highlight all the possible sources of capacitance between piston and cylinder: some are displacement dependent, $C_2(x)$, $C_3(x)$, $C_4(x)$, while others are fixed, C_1, C_5, and represent the point of contact between two elements and are usually separated by plastic materials in order to reduce friction. The total capacitance is given by (1). Substituting into (1) the equations for the capacitor with parallel and cylindrical surfaces, we obtain (2), which describes the relationship between displacement and capacitance, which appears nonlinear. Fig. 3 shows the relation between position and capacitance of (2). With the given mechanical dimensions, the largest contribution to the capacitance is given by the cylindrical capacitance between piston and cylinder, $C_2(x)$, and as long as the shock absorber is not fully compressed, the (2) can be simplified as (3). The sum of the fixed capacitances, $C_0 = C_1 + C_5$, can be experimentally computed by measuring the capacitance in full extension, and it is around a few hundred pF. The derivative of (3) provides information on the precision obtained in measuring the position given the precision in measuring the capacitance (4): assuming the same values for which Fig. 3 was made, the precision of $\pm$ 1 mm in the position measurement requires an error on the capacitance of $\pm$ 0.4 pF. Moreover, (4) shows that this correlation depends only on the ratio between the radius of the piston and cylinder and the dielectric constant of the oil.

$$C(x) = C_1 + C_5 + C_2(x) + C_3(x) + C_4(x) \tag{1}$$

$$C(x) = C_1 + C_5 + \frac{2\pi\varepsilon x}{ln\left(\frac{r_2}{r_1}\right)} + \frac{\pi(r_2 - r_1)^2\varepsilon}{l - x} + \frac{\pi r_3^2\varepsilon}{x} \tag{2}$$

$$C(x) \approx C_0 + \frac{2\pi\varepsilon}{ln\left(\frac{r_2}{r_1}\right)}x \tag{3}$$

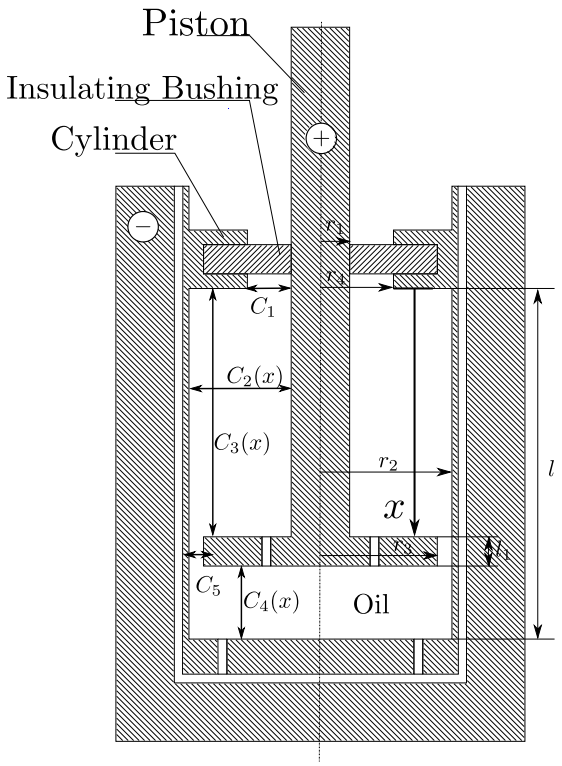

Fig. 2. Simplified shock absorber scheme to point out the capacitance equivalent model. x is the displacement; r_1, r_2, r_3, r_4, l, l_1 are mechanical dimensions; C_1, C_5 are fixed; $C_2(x)$, $C_3(x)$, $C_4(x)$ are displacement dependent; the cylinder is full of oil that works as dielectric. "+" and "-" represent the capacitor's terminals.

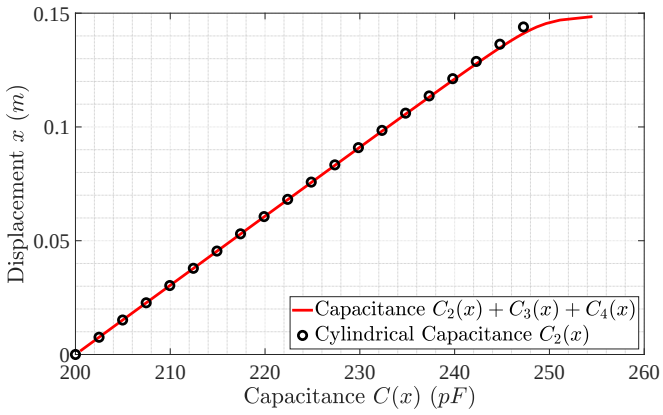

Fig. 3. Analytical capacitance-displacement characteristic: comparison between full model and simplified. Assuming $r_1 = 22\ mm$, $r_2 = 32\ mm$, $r_3 = 31.5\ mm$, $r_4 = 24\ mm$, $l = 160\ mm$, $l_1 = 10\ mm$ and as relative dielectric constant of the oil $\varepsilon = 2.2$; the point $x = 0$ show the value of the fixed capacitance C_0

$$\Delta C = \frac{2\pi\varepsilon}{ln\left(\frac{r_2}{r_1}\right)}\Delta x \tag{4}$$

III. Circuits to Measure Capacitance

In this section, the main circuits to measure an unknown capacitor are reported.

A. RC Circuit

The unknown capacitor, $C(x)$, is excited by two complementary switches; a voltage divider generates a threshold fed to a comparator alongside the capacitor's voltage, Fig. 4. Measuring the low time of the output square wave, t_1, the capacitance is estimated (5).

$$C(x) = \frac{t_1}{R_1 ln\left(\frac{V_{in}}{V_{in}-V_c(t_1)}\right)} \tag{5}$$

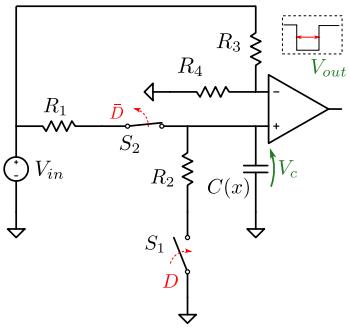

Fig. 4. Constant Voltage - RC Circuit

B. Constant Current Circuit

The unknown capacitor, $C(x)$, is excited with a triangular wave. A current monitor across resistor R_1 produces an output proportional to the capacitor current. A subtractor stage is used to remove the voltage offset, coming from the capacitance independent from the displacement shown in the previous section, Fig. 5. The capacitance value is given by (6), where $V_{out}(High)$ is the high level of the output of the subtractor stage, A_1 is the gain associated with the current monitor, and dV_{in}/dt is the slope of the input triangular wave.

$$C(x) = \frac{V_{out}(High)}{R_1 A_1 \frac{dV_{in}}{dt}} \tag{6}$$

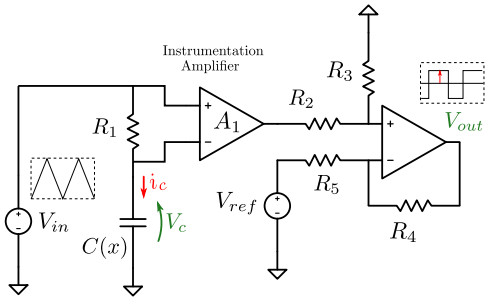

Fig. 5. Constant Current Circuit

C. Dual Slope Circuit

The constant current circuit can be modified by replacing the subtractor with an integrator, Fig. 6. When S_2 and S_3 are "ON", the integrator capacitor, C_1 is charged, whereas when S_1 and S_4 are "ON", C_1 is discharged. Comparing the voltages

differences of the two phases of the charge and discharge on the integrator capacitor gives (7), where A_1 is the gain of the current monitor, t_f is the discharging time of C_1, t_r is the charging time of C_1. $Q_{C_x}(t_r)$ is the charge of the unknown capacitor $C(x)$ at the time t_r: this quantity can also be written as $Q_{C_x}(t_r) = C(x)V_c(t_r)$, and comes from the integration of the current on the unknown capacitor. By measuring t_f and $V_c(t_r)$ the capacitance is estimated as (8).

$$\frac{A_1 R_1 Q_{C_x}(t_r)}{R_3 C_1} = \frac{V_{ref} t_f}{R_3 C_1} \tag{7}$$

$$C(x) = \frac{V_{ref} t_f}{V_c(t_r) A_1 R_1} \tag{8}$$

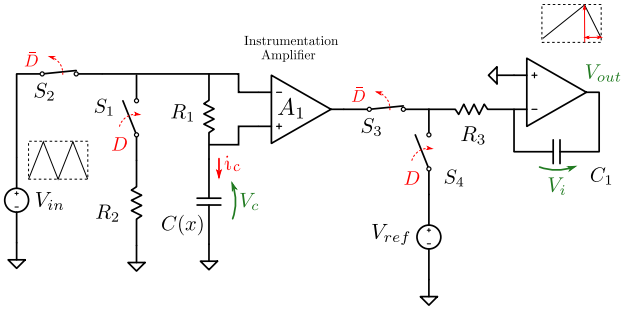

Fig. 6. Dual Slope Integrator Circuit

D. Astable Multivibrator Circuit

The output of the operational amplifier charges the unknown capacitor, its voltage is compared with two thresholds produced by the positive feedback of the operational amplifier Fig. 7. A constant voltage V_{in} generates asymmetric thresholds so that the operational amplifier can be used with a single-supply configuration. Setting $R_1 = R_3 = R_4$ and neglecting the non-idealities of the amplifier, the unknown capacitor can be calculated as (9), where $f(x)$ is the output frequency.

$$C(x) = \frac{1}{R_2 f(x) ln(4)} \tag{9}$$

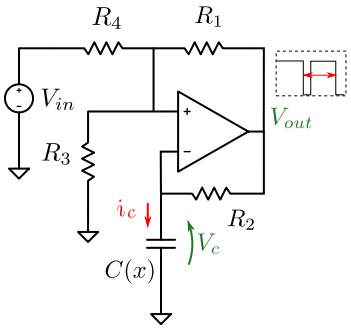

Fig. 7. Single Supply Astable Multivibrator Circuit

IV. Astable Multivibrator Stage: Design Methodology

In this article, it is used the astable multivibrator topology. This circuit is chosen over the other presented because of its simplicity: it does not require switches or a waveform generator, plus it has a single supply feature. These advantages make it possible to create a smaller and cheaper sensor. A working frequency of hundreds of kHz is required to have a good dynamic response. The measure of the capacitance, and hence displacement, is given by the astable output's high and low state time (10 - 11). Where V_h and V_l are the two output levels of the operational amplifier, V_{th}^+ and V_{th}^- are the two threshold voltages on the non-inverting input, which, using the superposition principle, can be computed as (12 - 13).

$$t_1 = R_2 C(x) ln\left(\frac{V_{th}^- - V_h}{V_{th}^+ - V_h}\right) \tag{10}$$

$$t_2 = R_2 C(x) ln\left(\frac{V_{th}^+ - V_l}{V_{th}^- - V_l}\right) \tag{11}$$

$$V_{th}^+ = V_{in}\left(\frac{R_1||R_3}{R_4 + R_1||R_3}\right) + V_h\left(\frac{R_4||R_3}{R_1 + R_4||R_3}\right) \tag{12}$$

$$V_{th}^- = V_{in}\left(\frac{R_1||R_3}{R_4 + R_1||R_3}\right) + V_l\left(\frac{R_4||R_3}{R_1 + R_4||R_3}\right) \tag{13}$$

The oscillation frequency is then given by the sum of the time needed to reach the thresholds (14).

$$f(x) = \frac{1}{t_1 + t_2} \tag{14}$$

The capacitor value can be computed substituting (12 - 13) into (14):

$$C(x) = \frac{1}{R_2 \cdot f \cdot ln\left(\frac{V_{th}^+ - V_l}{V_{th}^- - V_l}\frac{V_{th}^- - V_h}{V_{th}^+ - V_h}\right)} \tag{15}$$

In practice, to avoid overestimating the oscillation frequency, non-idealities must be taken into account. The capacitor, $C(x)$, is not charged with a fixed voltage equal to V_h, but it is affected by the slew rate of the amplifier, as well as in the discharge phase. Because of the slew rate, the capacitor voltage exhibits an overshoot, Fig. 8: as long as the voltage output is not less than the capacitor voltage, the capacitor continues to charge, and vice versa. Therefore, the differential equation describing the capacitor voltage is (16), whose solution is (17), where s_r is the slew rate of the operational amplifier, and $\lambda = t/(R_2 C(x))$.

$$\frac{dV_c}{dt} = \frac{1}{R_2 C(x)}\left(s_r t - V_c\right) \tag{16}$$

$$V_c(\lambda) = e^{-\lambda}\left(V_c(t_0) + s_r R_2 C(x)\left(e^{\lambda}\left(\lambda - 1\right) + 1\right)\right) \tag{17}$$

Moreover, there is a delay, T_{delay}, between the time when the voltage on the capacitor exceeds the voltage given by

the voltage divider on the non-inverting gate and the time when the operational amplifier changes its output, Fig. 8. This effect is associated with the time required to charge the parasitic capacitance on the operational amplifier's inputs and the component's group delay. In order to compensate for this error, the slope of the operational amplifier charging and discharging curve is evaluated and used to correct the thresholds (18 - (19).

$$V^{+}_{th_{cr}}(C(x)) = V^{+}_{th} + T_{delay}\frac{dV_c}{dt}\bigg|_{t=0,\ V_c(0)\approx V^{-}_{th}} \tag{18}$$

$$V^{-}_{th_{cr}}(C(x)) = V^{-}_{th} - T_{delay}\frac{dV_c}{dt}\bigg|_{t=0,\ V_c(0)\approx V^{+}_{th}} \tag{19}$$

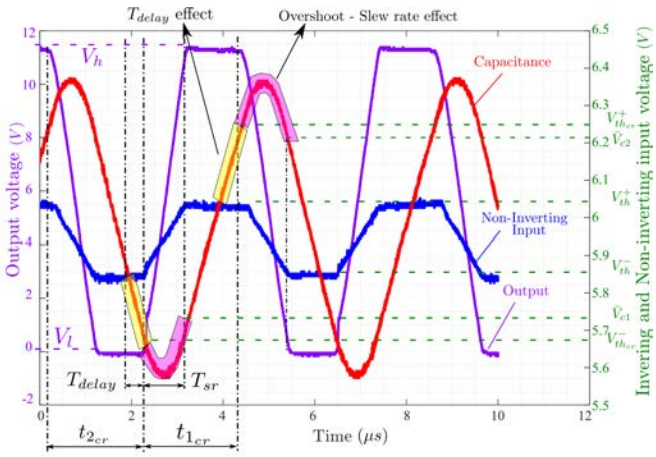

Fig. 8. Measured voltages on the non-inverting port, inverting port, and output of the oscillator stage with $C(x) = 255\ pF$. The frequency measured by the oscilloscope is around $239\ kHz$.

Thus the frequency is computed using the two corrected times $t_{1_{cr}}$ and $t_{2_{cr}}$, (20) and (21), to take into account the non-linearities: overshoot phenomena, response delay and slew rate. The initial capacitor voltage is calculated using the differential equation (16) as shown in (22) and (23). Also, the final voltage reached by the capacitor it is calculated using (18) and (19). At last, there is the parameter T_{sr} that is equal to $(V_h - V_l)/s_r$.

$$t_{1_{cr}}(x) = R_2 C(x) ln\left(\frac{\bar{V}_{c1}(C(x)) - V_h}{V^{+}_{th_{cr}}(C(x)) - V_h}\right) + T_{sr} \tag{20}$$

$$t_{2_{cr}}(x) = R_2 C(x) ln\left(\frac{\bar{V}_{c2}(C(x)) - V_l}{V^{-}_{th_{cr}}(C(x)) - V_l}\right) + T_{sr} \tag{21}$$

$$\bar{V}_{c1}(x) = V_c\left(\lambda = \frac{T_{sr}}{R_2 C(x)}, V_c(\lambda = 0) = V^{-}_{th_{cr}}\right) \tag{22}$$

$$\bar{V}_{c2}(x) = V_c\left(\lambda = \frac{T_{sr}}{R_2 C(x)}, V_c(\lambda = 0) = V^{+}_{th_{cr}}\right) \tag{23}$$

The comparison between the ideal, the measured, and the corrected frequency is represented in Fig. 9. The ideal equations cannot describe the behavior of the multivibrator stage for the frequencies of interest; whereas using the corrections, the match with the experimental observations improves.

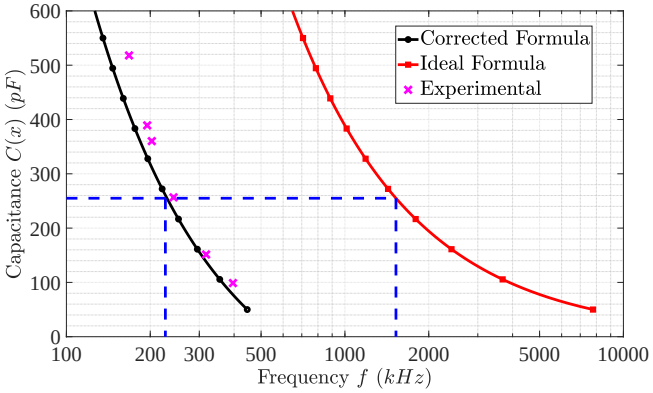

Fig. 9. Frequency-capacitance characteristics; squares (red): ideal formula; circles (black): corrected formula; crosses (purple): experimental. Example: with $C = 250\ pF$, experimental oscillation frequency = $242\ kHz$; ideal oscillation frequency = $1.525\ MHz$; corrected oscillation frequency = $227\ kHz$.

In the case where the change in capacitance along the stroke of the piston, is a couple of hundred pF, as suggested in Fig. 3, it is possible to linearize the characteristic that connects capacitance and frequency. The characteristic can be linearized around the capacitance, $\bar{C}$, which represents the capacitance when the piston is positioned at half its stroke. Combining the two linear functions: the position-capacitance function, $x = b_1 C + b_2$, and the capacity-frequency function, $C = a_1 f + a_2$, we obtain the final input-output characteristic (24) that connects position and measured frequency. Where x is the displacement, f is the oscillation frequency, and the coefficients are expressed in (25 - 28).

$$x = (b_1 a_1) f + (b_2 + b_1 a_2) \tag{24}$$

$$b_1 = \frac{ln\left(\frac{r_2}{r_1}\right)}{2\pi\varepsilon} \tag{25}$$

$$b_2 = -\frac{C_0 ln\left(\frac{r_2}{r_1}\right)}{2\pi\varepsilon} \tag{26}$$

$$a_1 = \frac{1}{\frac{df_{cr}(C)}{dC}\Big|_{\bar{C}}} \tag{27}$$

$$a_2 = \bar{C} - \frac{f_{cr}(\bar{C})}{\frac{df_{cr}(C)}{dC}\Big|_{\bar{C}}} \tag{28}$$

The term $b_2 + b_1 a_2$ is an offset; the gain between frequency and position is given by $b_1 a_1$. The coefficient b_1 depends only on the mechanical quantities. The sensitivity between

frequency and position can be adjusted by changing the coefficient a_1 expressed as $pF\ /\ kHz$. By acting on a_1 it is possible to increase the frequency range, Δf, which corresponds to the same ΔC, namely Δx, Fig. 10. The increase in sensitivity is paid for by a smaller range in which linearization is effective.

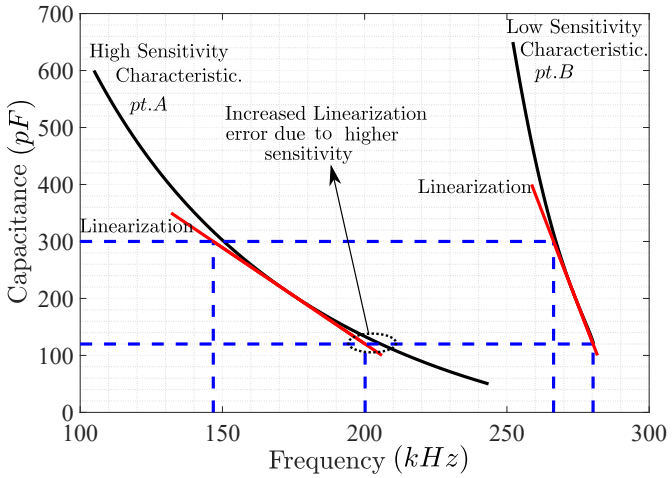

Fig. 10. Trade off between high and low sensitivity, the high sensitivity characteristic presents with the same $\Delta\ C$ a greater interval $\Delta\ f$ but on the boundaries of the interval $\Delta\ C$ the linearized characteristic presents a bigger error, reducing the domain in which can be used.

In Fig. 11, a_1 is computed with respect to the resistor network; on the x-axis is represented the value of the negative feedback resistor, R_2, which governs the speed of the RC transient, while the y-axis shows the ratio of the positive feedback resistors, R_1/R_3, responsible of the thresholds. $R_3 = R_4$ was imposed to simplify the analysis. The high-sensitivity characteristic in Fig. 10 is represented with a cross, $pt.A$, while the low-sensitivity characteristic, with a circle, $pt.B$. Larger values of a_1 are obtained for low values of the ratio R_1/R_3 and by increasing the feedback resistor R_2.

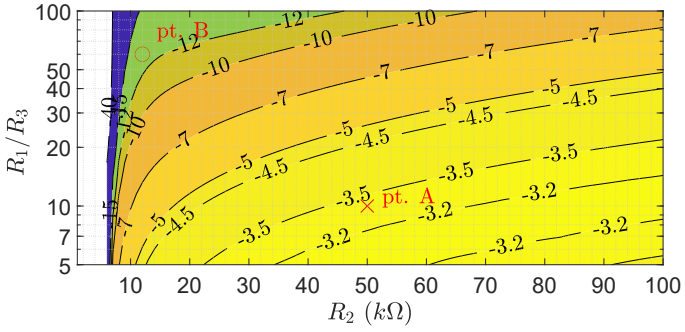

Fig. 11. Coefficient a_1 (pF/kHz) as a function of the resistive network with a fixed capacitance of 210 pF and $R_3 = R_4$; y-axis is in logarithmic scale.

Fig. 12 shows the dependence of the oscillation frequency with respect to the resistor network: the increase in sensitivity is matched by a decrease in the oscillation frequency, with a possible effect on the sensor dynamics, and a reduction of the available samples per second.

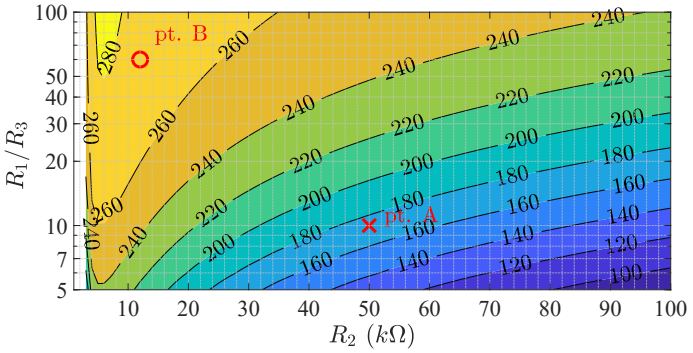

Fig. 12. Output frequency (kHz) as a function of the resistive network with a fixed value of capacitance of 210 pF and $R_3 = R_4$; y-axis is in logarithmic scale.

In Fig. 13, the coefficient a_1 is computed with respect to slew-rate, s_r, and the delay, T_{delay}. The highest sensitivity is obtained with a slight delay and a high slew rate, although increasing the slew rate above a certain threshold becomes irrelevant for the purpose of increasing sensitivity.

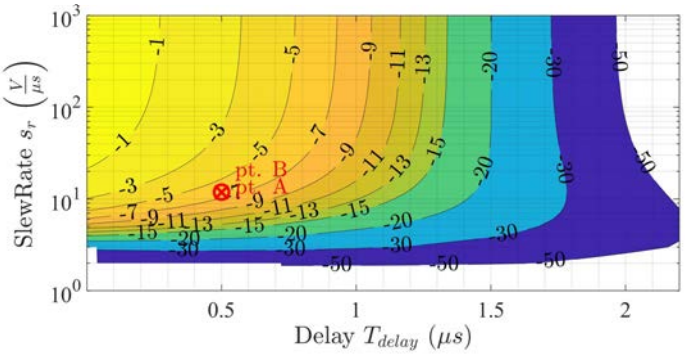

Fig. 13. Coefficient a_1 (pF/kHz) as a function of delay, T_{delay}, and slew rate, s_r, with a fixed value of capacitance of 210 pF; y-axis is in logarithmic scale.

V. Acquisition Pipeline

In order to estimate the frequency, namely the displacement, a double interrupt is set on both rising and falling edges and using the clock counter. The frequency of the output signal of the astable, f_{osc}, is estimated as (29), where f_{clk} is the microcontroller clock frequency, $\text{cnt}_{clk}(k)$ is the current value of the counter and $\text{cnt}_{clk}(k-1)$ is the previous one.

$$f_{osc} = \frac{f_{clk}}{\text{cnt}_{clk}(k) - \text{cnt}_{clk}(k-1)} \tag{29}$$

Triggering the interrupt on both rising and falling edges allows a consistency check: if the two measurements are equal, the mean of the two values is performed. Another mean over j samples is used to reduce the output frequency from the hundreds of kHz range to hundred of Hz range in accordance with the communication bus frequency limit. Adding a rolling-median and a low pass filter as additional conditioning is

possible, but experimental results suggest that there is not any added value. Eventually, the conversion between frequency and displacement is performed. This conversion is done through the linearized function described before and the parameters, gain and offset, can be adjusted during a tuning procedure. A Fourier transform of the typical oscillation of a shock absorber is shown in Fig. 14: the maximum dynamics is around 20 Hz. This sets a constrain for the sensor's dynamic response, and it is used as a boundary on the sample time and the value of j given the oscillation frequency measured. In this article, the value of desired output frequency for acquisition is set to 50 Hz, and the sensor measurement is sent and acquired via CAN bus.

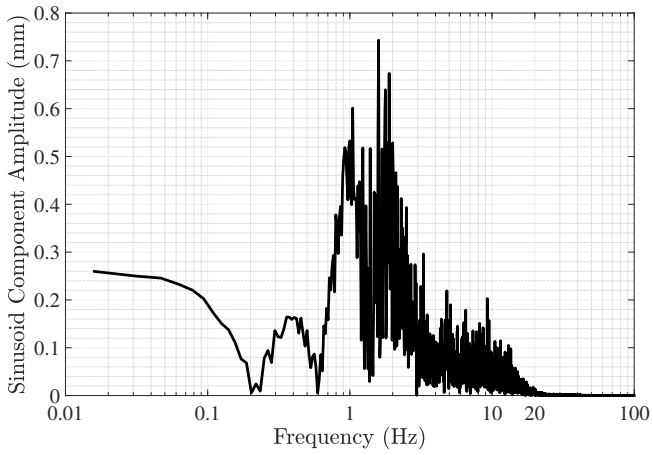

Fig. 14. Fast Fourier Transform (FFT) of a shock absorber displacement

VI. Experimental Data and Sensor Validation

Experimental validation is done in Marelli Ride Dynamics facilities, first using a production test bench and later on a demo car. Fig. 15 shows the vehicle equipped with the developed prototype and a reference sensor, Hella 60667364. The reference sensor output is a voltage from 0 to 5 V proportional to an angle between -40^o and 40^o; it is mounted on the vehicle to have a direct correlation between the measured angle and the displacement of the shock absorber. Fig. 16 shows the characteristic between the angle and the piston rod displacement. The developed prototype measures 56x32x38 mm casing included, Fig. 18; the connection to the rod and the external cylinder are made with cables. During these tests, microcontroller with a clock frequency of 600 MHz was used; however, we also tested lower clock frequencies without degrading performance. The measurements are acquired through a CAN bus. Fig. 17 shows linear characteristic between frequency and displacement of the developed prototype; a displacement variation of 60 mm corrisponds to a frequency variation of 6 kHz.

Fig. 15. Democar setting: developed prototype mounted directly on the shock absorber and reference sensor mounted to have a measure proportional to the rod displacement.

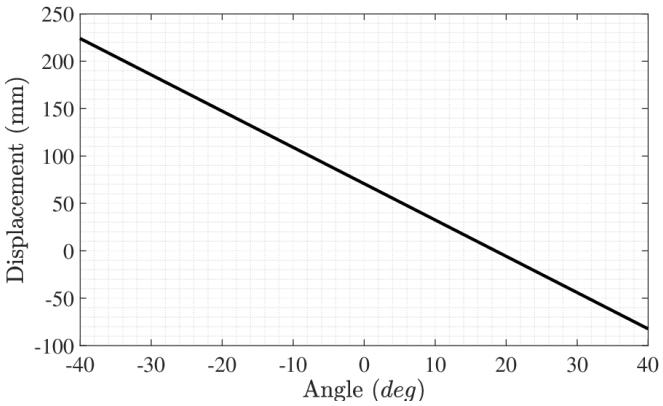

Fig. 16. Reference sensor, Hella 60667364, Angle - Vertical position characteristic

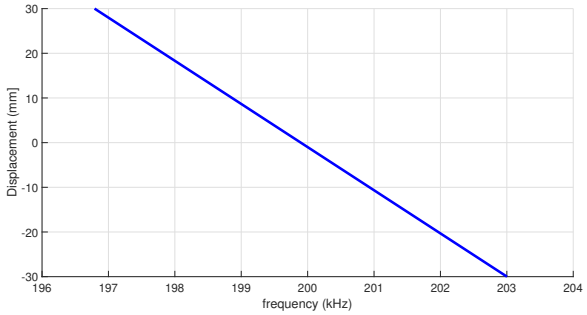

Fig. 17. Developed prototype: linear characteristic between frequency and displacement.

References

[1] A. Dorneich and M. Fritton, "Microwave position sensor for hydraulic drives," *Procedia Engineering*, vol. 168, pp. 1257–1260, 2016.

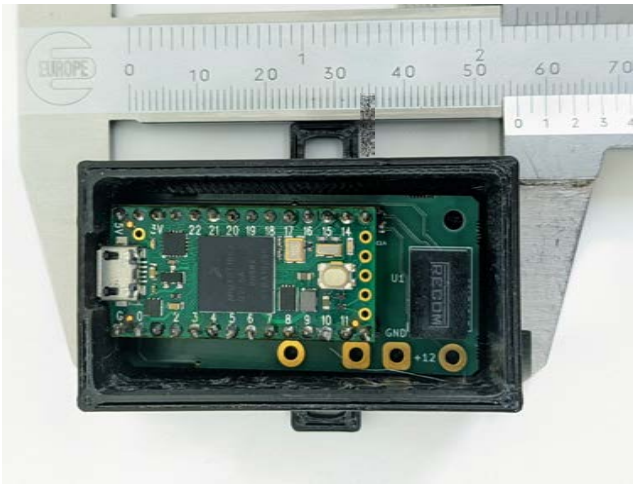

Fig. 18. Developed prototype with 3D printed case; dimensions 56x32x38 mm casing included

[2] S. Fericean, A. Hiller-Brod, A. Dorneich, M. Fritton, J. Büchler, and T. Holzschuh, "Development of a microwave displacement sensor for hydraulic devices," in *SENSORS, 2011 IEEE*. IEEE, 2011, pp. 2042–2045.

[3] S. Fericean, A. Hiller-Brod, A. D. Dorneich, and M. Fritton, "Microwave displacement sensor for hydraulic devices," *IEEE Sensors Journal*, vol. 13, no. 12, pp. 4682–4689, 2013.

[4] P. Ripka, *Magnetic sensors and magnetometers*. Artech house, 2021.

[5] P. Ripka, A. Chirtsov, M. Mirzaei, and J. Vyhnanek, "Inductance position sensor for pneumatic cylinder," *AIP Advances*, vol. 8, no. 4, p. 048001, 2018.

[6] M. De Volder, J. Coosemans, R. Puers, and D. Reynaerts, "Characterization and control of a pneumatic microactuator with an integrated inductive position sensor," *Sensors and Actuators A: Physical*, vol. 141, no. 1, pp. 192–200, 2008.

[7] P. Ripka, J. Blažek, M. Mirzaei, P. Lipovskỳ, M. Šmelko, and K. Draganová, "Inductive position and speed sensors," *Sensors*, vol. 20, no. 1, p. 65, 2020.

[8] A. Grima, M. Di Castro, A. Masi, and N. Sammut, "Design enhancements of an ironless inductive position sensor," *IEEE Transactions on Instrumentation and Measurement*, vol. 69, no. 4, pp. 1362–1369, 2019.

[9] T. Hojnik, P. Flick, and J. Roberts, "Contactless position sensing and control of pneumatic cylinders using a hall effect sensor array," in *Proceedings of the Australasian Conference on Robotics and Automation 2017*. Australian Robotics and Automation Association, 2017, pp. 1–8.

[10] P. Ripka, A. Chirtsov, and V. Grim, "Contactless piston position transducer with axial excitation," *IEEE Transactions on Magnetics*, vol. 53, no. 11, pp. 1–4, 2017.

[11] P. Ripka, M. Mirzaei, A. Chirtsov, and J. Vyhnanek, "Transformer position sensor for a pneumatic cylinder," *Sensors and Actuators A: Physical*, vol. 294, pp. 91–101, 2019.

[12] M. Mirzaei, P. Ripka, and V. Grim, "A novel position sensor with a conical iron core," *IEEE Transactions on Instrumentation and Measurement*, vol. 69, no. 11, pp. 9178–9189, 2020.

[13] D. Rybarczyk, "Application of the mems accelerometer as the position sensor in linear electrohydraulic drive," *Sensors*, vol. 21, no. 4, p. 1479, 2021.

[14] "Stossdampefer mit einrichtung zur langenmessung," Germany Patent DE3 518 858A1, Nov. 1985.

[15] A. D.-I. E. D.-I. M. D.-I. Thürigen, "Position detection device for a fluid cylinder," European Patent Office Patent EP2 149 715B1, Feb. 2009.

[16] L. M. Comella, K. Ayvazov, T. Cuntz, A. Van Poelgeest, J. Schächtele, and J. Stallkamp, "Characterization of a capacitive position sensor for a miniaturized hydraulic actuator," *IEEE Sensors Journal*, vol. 17, no. 1, pp. 113–120, 2016.

[17] T. Pawlenka and J. Škuta, "Shaft displacement measurement using capacitive sensors," in *2021 22nd International Carpathian Control Conference (ICCC)*. IEEE, 2021, pp. 1–5.